Review of Scientific Instruments

RESEARCH ARTICLE | MARCH 25 2025

Development of density measurement at high pressure and high temperature using the x-ray absorption method combined with laser-heated diamond anvil cell

Hidenori Terasaki ; Hiroyuki Kamina; Saori I. Kawaguchi ; Tadashi Kondo ; Ko Morioka; Ryo Tsuruoka ; Moe Sakurai ; Akira Yoneda ; Seiji Kamada ; Naohisa Hirao

Rev. Sci. Instrum. 96, 033907 (2025)
https://doi.org/10.1063/5.0223133

AIP Publishing

Review of Scientific Instruments ARTICLE pubs.aip.org/aip/rsi

Development of density measurement at high pressure and high temperature using the x-ray absorption method combined with laser-heated diamond anvil cell

Cite as: Rev. Sci. Instrum. 96, 033907 (2025); doi: 10.1063/5.0223133
Submitted: 12 June 2024 • Accepted: 25 February 2025 •
Published Online: 25 March 2025

Hidenori Terasaki,[1,a)] Hiroyuki Kamina,[1] Saori I. Kawaguchi,[2] Tadashi Kondo,[3] Ko Morioka,[1] Ryo Tsuruoka,[3] Moe Sakurai,[1] Akira Yoneda,[3] Seiji Kamada,[4] and Naohisa Hirao[2]

AFFILIATIONS

[1] Department of Earth Sciences, Okayama University, Tsushimanaka 3-1-1, Kita-ku, Okayama 7008530, Japan
[2] Japan Synchrotron Radiation Research Institute, SPring-8, Koto 1-1-1, Sayo-cho, Sayo-gun, Hyogo 6795198, Japan
[3] Department of Earth and Space Science, Osaka University, Machikaneyama-cho 1-1, Toyonaka, Osaka 5600043, Japan
[4] AD Science Incorporation, Hon-cho 2-2-7, Funabashi, Chiba 2730005, Japan

[a)] **Author to whom correspondence should be addressed:** tera@okayama-u.ac.jp

ABSTRACT

The densities of liquid materials at high pressures and high temperatures are important information to understand the elastic behavior of liquids at extreme conditions, which is closely related to the formation and evolution processes of the Earth and planetary interiors. The x-ray absorption method is an effective method to measure the density of non-crystalline materials at high pressures. However, the temperature condition of the x-ray absorption method using a diamond anvil cell (DAC) has been limited to 720 K to date. To significantly expand the measurable temperature condition of this method, in this study, we developed a density measurement technique using the x-ray absorption method in combination with a laser-heated DAC. The density of solid Ni was measured up to 26 GPa and 1800 K using the x-ray absorption method and evaluated by comparison with the density obtained from the x-ray diffraction. The density of solid Ni with a thickness >17 μm was determined with an accuracy of 0.01%–2.2% (0.001–0.20 g/cm^3) and a precision of 0.8%–1.8% (0.07–0.16 g/cm^3) in the x-ray absorption method. The density of liquid Ni was also determined to be 8.70 ± 0.15–8.98 ± 0.38 g/cm^3 at 16–23 GPa and 2230–2480 K. Consequently, the temperature limit of the x-ray absorption method can be expanded from 720 to 2480 K by combining it with a laser-heated DAC in this study.

I. INTRODUCTION

Density is one of the most fundamental and indispensable physical properties for understanding the interior structures of the Earth and planets and their formation and evolution processes. The densities of liquids, such as silicate melts and liquid iron alloys, at high pressures and high temperatures are closely related to the dynamics and differentiation of planetary interiors. For instance, the density of silicate melts determines the ascent/descent behavior of magma in solid mantle and differentiation between magma and coexisting crystals in the magma ocean or magma chamber (e.g., Ref. 1). The density of liquid iron-alloys controls the convection behavior of the liquid core, which drives the planetary dynamo, and also controls the core crystallization scenario and core structure (e.g., Ref. 2).

There are several methods that can measure the density of non-crystalline materials (liquids and glasses) at high pressures and high temperatures.[3] The x-ray absorption method and the x-ray diffraction method are effective methods to measure the density of non-crystalline materials, especially at very high pressures. In the x-ray absorption method developed by Katayama *et al.*,[4] density is obtained from the measured x-ray transmission from the sample. Densities of liquid iron-alloys (e.g., Refs. 5 and 6) and silicate melts (e.g., Ref. 1) have been measured using this method with a large

volume press up to 10 GPa. In the measurements at higher pressures, a diamond anvil cell (DAC) was used, and the density of silicate glasses was measured up to 127 GPa at room temperature.[7,8] The measurement with DAC at high temperatures was carried out using an externally heated (EH) DAC up to 720 K.[9–11] The uncertainty of the measured density in this method ranges from 1.1%–4.3% at room temperature and 0.2%–2.0% at high temperatures. However, the temperature conditions that can be generated using the EH-DAC are far insufficient for the temperature of planetary cores, for example, 2100–2300 or 2800–3100 K for the Martian core.[12]

In the x-ray diffraction method, density can be obtained via pair distribution function analyses of x-ray diffuse scattering signals from the non-crystalline samples.[13] Recent measurements using this method combined with laser-heated DAC reported densities of liquid Fe, Fe–Ni–alloys up to 116 GPa and 4350 K[14–16] and those of liquid silicate (basalt) up to 60 GPa and 3273 K.[17] The uncertainty of the density in this method ranges from 0.7%–5.4% for liquid Fe–Ni–alloys and 1.2%–1.9% for liquid basalt. The measurable temperature conditions of the x-ray diffraction method are much higher than those of the x-ray absorption method. However, the x-ray absorption method has the major advantage that density can be determined more simply and directly from the x-ray transmission data of a sample and does not require any sophisticated analytical procedures and/or assumptions. Therefore, if the measurable temperature condition of the x-ray absorption method can be extended to much higher temperature, densities of various liquids under high pressures are accessible more easily. This leads to progress in understanding the elastic behavior of liquids at extreme conditions and also in understanding accurate behaviors of silicate magma and liquid iron-alloys in planetary deep interiors.

In this study, we developed density measurements using the x-ray absorption method in combination with a laser-heated DAC to expand the measurable temperature conditions significantly. The density of solid Ni was measured, and the accuracy and precision of the obtained density were evaluated by comparing with the density measured from x-ray diffraction. Density measurements for liquid Ni were also performed using the same setup.

II. EXPERIMENTAL METHOD

A. X-ray absorption method

The sample density was obtained using the x-ray absorption method. In this method, the x-ray transmittance through a material [the intensity ratio of the transmitted (I_1) and incident x rays (I_0)] can be described by the Lambert–Beer law as follows:

$$I_1/I_0 = \exp(-\mu\rho t), \tag{1}$$

where μ, ρ, and t represent the mass absorption coefficient, density, and thickness in the x-ray direction of a material, respectively. The used cell assembly in a DAC is shown in Fig. 1(a).

In the cell assembly, sample and reference materials are sandwiched by pressure medium in the sample chamber. The reference material is used to obtain sample thickness following the methods by Refs. 7 and 9. X-ray transmittance through a sample and a reference material is expressed, respectively, as

$$I_s/I_0 = \exp(-\mu_s\rho_s t_s - \mu_{PM}\rho_{PM}t_{PM} - \mu_{dia}\rho_{dia}t_{dia}), \tag{2}$$

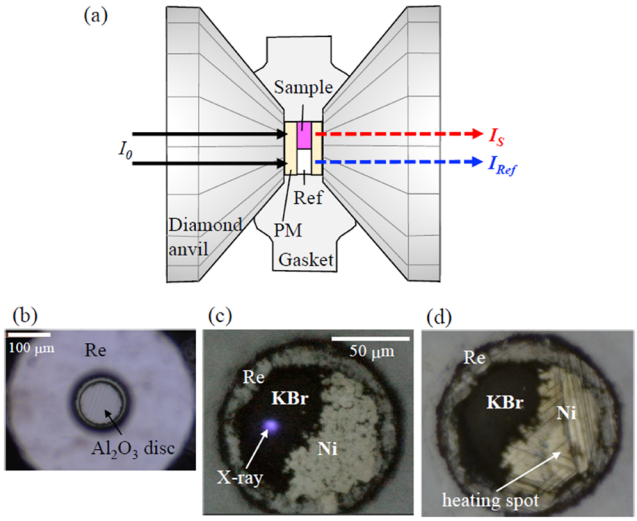

FIG. 1. (a) Schematic image of cell assembly and x-ray paths. Ref and PM indicate reference material (KBr) and pressure medium (Al_2O_3 or KBr), respectively. I_0, I_S, and I_{ref} represent intensities of incident x-ray, transmitted x-ray through the sample, and that through the reference material, respectively. (b) Optical microscope image of a single crystal Al_2O_3 disk in the Re gasket. The diameter of the disk was 5–10 μm smaller than that of the sample hole in the gasket. (c) Reflecting optical microscope image of the sample and reference through diamond anvil before heating (CCH04). Bright and dark areas represent Ni and KBr, respectively. The surrounding part is a Re gasket. X ray can also be seen as a bright spot. (d) Reflecting optical microscope image of the sample and reference after second heating (CCH04). The heating spot can be seen in the Ni as a circular area after heating.

$$I_{ref}/I_0 = \exp(-\mu_{ref}\rho_{ref}t_{ref} - \mu_{PM}\rho_{PM}t_{PM} - \mu_{dia}\rho_{dia}t_{dia}), \tag{3}$$

where subscripts s, ref, PM, and dia indicate sample, reference material, pressure medium, and diamond anvil, respectively. When we assume $t_s = t_{ref} \equiv t$, the second and third terms of the right hand side of Eqs. (2) and (3) can be canceled out by dividing Eq. (2) by Eq. (3), written as

$$\frac{(I_s/I_0)}{(I_{ref}/I_0)} = \exp\left[\left(-\mu_s\rho_s + \mu_{ref}\rho_{ref}\right)t\right]. \tag{4}$$

Then, t can be described as

$$t = \frac{1}{-\mu_s\rho_s + \mu_{ref}\rho_{ref}} \ln\left[\frac{(I_s/I_0)}{(I_{ref}/I_0)}\right] = \frac{1}{-\mu_s\rho_s^{XRD} + \mu_{ref}\rho_{ref}^{XRD}} \ln\left[\frac{(I_s/I_0)}{(I_{ref}/I_0)}\right], \tag{5}$$

where ρ_s^{XRD} and ρ_{ref}^{XRD} are densities of the sample and reference determined from the lattice volumes from X-ray diffraction (XRD) measurement, respectively. The measured x-ray transmittance of the sample and reference were used for I_s/I_0 and I_{ref}/I_0, respectively. The μ_s and μ_{ref} values were taken from the database of the National Institute of Standards and Technology (https://dx.doi.org/10.18434/T48G6X). In this study, t was determined using the XRD and transmittance data after quenching in

each heating cycle. Then, the sample density from the x-ray absorption method (ρ_s^{Abs}) at high temperature can be obtained from Eqs. (4) and (5) as

$$\rho_s^{Abs} = \frac{1}{\mu_s}\left[\mu_{ref}\rho_{ref}^{XRD} - \frac{1}{t}\ln\left\{\frac{(I_s/I_0)}{(I_{ref}/I_0)}\right\}\right]. \quad (6)$$

The x-ray transmittance of the sample was measured at high temperature.

B. Measurements

Density measurements using the x-ray absorption method were carried out at the BL10XU beamline of the SPring-8 synchrotron facility (Sayo, Japan).[18] A schematic representation of the experimental setup at the BL10XU is shown in Fig. 2. A monochromatic x-ray beam was tuned to 30 keV using a Si(111) and Si(220) double-crystal monochromator. The available x-ray energy range on the BL10XU beamline is 6–61 keV. The x-ray energy range of 20–30 keV is suitable for the x-ray transmittance of the samples and surrounding materials of this study. For the XRD measurement, diffraction peaks can be collected at wider diffraction angles using higher x-ray energy. Therefore, we used an x ray of 30 keV in this study. The x-ray beam was collimated, and its representative size of full width at half maximum was ~10 μm. The I_0 and I_1 were measured using ion chambers as shown in Fig. 2. In each measurement, I_0 and I_1 were measured ten times to evaluate the intensity variations (i.e., measurement errors) in I_0 and I_1, and average values were used. The exposure time for one measurement was set to 1 s; therefore, time for ten measurements took 10 s. The dark current of the ion chambers was measured as the background. The dark current background was subtracted from the raw x-ray intensities. Subsequently, x-ray transmittance was obtained from the ratio of I_1/I_0. To check the linearity of x-ray sensitivity of the detectors used in this study, the relationships between measured transmittance $[(I_1/I_0)_{obs}]$ and calculated transmittance $[(I_1/I_0)_{cal}]$ were checked using various metallic foils (Al, Fe, Cu, Ag, In, and Pt) with known thicknesses and densities based on XRD measurements. $(I_1/I_0)_{obs}$ and $(I_1/I_0)_{cal}$ show a linear relation with a slope of 1.002(6) with R = 0.9986.

XRD measurements were conducted using a flat panel detector (XRD0822 CP23, PerkinElmer, Inc. or XRD1611 CP3, Varex Imaging, Corp.) with an exposure time of 1–2 s to determine the ρ_{ref} and also ρ_s to determine the experimental pressures. IPAnalyzer and PDIndexer software[19] were used to convert the two-dimensional XRD patterns into one-dimensional (1D) XRD profiles and to analyze 1D XRD profiles, respectively. The experimental pressures at 300 K were determined from the lattice volumes of the sample (Ni) and reference (KBr) and their EOSs.[20,21] The experimental pressures at high temperatures were determined from the lattice volume of Ni and its EOS.[22]

C. Cell assembly and high P–T experiments

High pressure experiments were carried out using a symmetric DAC. The culet sizes of the diamond anvils used were 400, 450, 550, and 600 μm. The sample and reference materials were Ni (99.99% purity, RARE METALLIC Co., Ltd.) and KBr (99.9% purity, Wako Pure Chemicals Industries, Ltd), respectively. The sample and reference were pelletized with initial thicknesses of 15–40 μm, and cut pellets were placed in a hole of the Re gasket. The sample and reference were sandwiched between the pressure medium (Al_2O_3 disk or KBr pellet) as shown in Fig. 1(a). The pressure medium used for each run is listed in Table I (cell type A: Al_2O_3 disk, B: KBr pellet). The Al_2O_3 disk was a single crystal disk with a thickness of 25 or 35 μm and with a mirror polished flat surface. The disk was cut to a diameter of 5–10 μm smaller than the sample hole diameter [Fig. 1(b)] using an UV-laser micro-cutting system (wavelength of 349 nm, Spectra-Physics, Inc.) with a laser size of 5 μm. The KBr pellet with a thickness of ~40 μm was cut to a hexagonal or octagonal shape to fit a sample hole of the gasket. A Re gasket was pre-indented to 60–90 μm in thickness and has a sample hole of 90–150 μm in diameter.

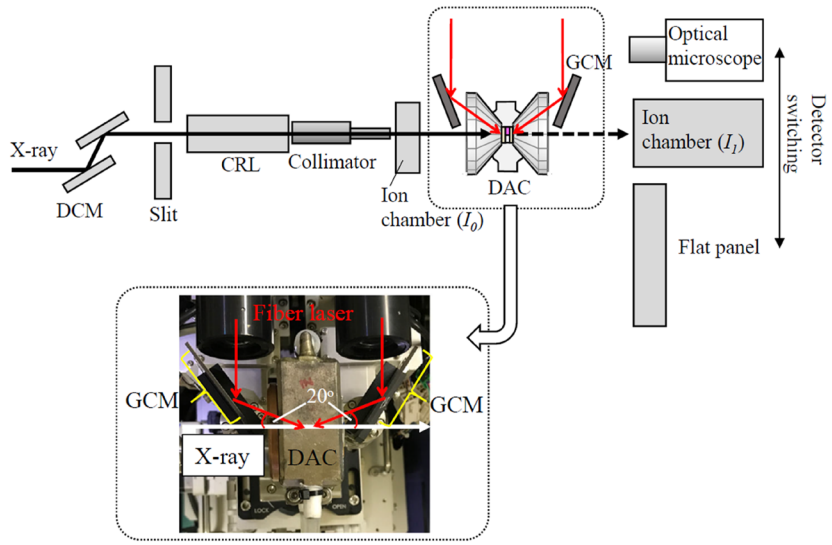

FIG. 2. Schematic image of the setup of density measurement at the BL10XU beamline. The x-ray was monochromatized to 30 keV using a double-crystal monochromator (DCM). The x-ray was collimated with a diameter of ~10 μm using a compound refractive lens (CRL) and collimator and introduced to DAC. The dashed arrow indicates the transmitted x-ray through the sample or reference material. Detectors can be switched by moving the detector stages. The inset image shows the double-sided laser heating with an oblique angle of 20°. Red arrows show fiber lasers. By this tilting-laser setup, the glassy carbon mirror (GCM) for laser heating did not block the x-ray path.

TABLE I. Experimental conditions and density results.

Run No.	Cell type[a]	Heat cycle[b]	P(Ni)[c] (GPa)	σ[P(Ni)][d] (GPa)	P(KBr)[e] (GPa)	σ[P(KBr)] (GPa)	T_{Abs} (K)	$\sigma(T_{Abs})$ (K)	T_{XRD} (K)	$\sigma(T_{XRD})$ (K)	$(I_s/I_0)/(I_{ref}/I_0)$	$\sigma[(I_s/I_0)/(I_{ref}/I_0)]$	ρ_s^{Abs} (g/cm^3)	$\sigma(\rho_s^{Abs})$ (g/cm^3)	ρ_s^{XRD} (g/cm^3)	$\sigma(\rho_s^{XRD})$ (g/cm^3)
Solid Ni																
CCH04	A	H1	12.5	0.3			1525	25	1540	20	0.9097	0.0003	8.989	0.133	8.954	0.006
CCH04	A	H1	11.4	0.4			1490	40	1480	30	0.9110	0.0003	8.930	0.138	8.928	0.010
CCH04	A	H2	11.6	0.3			1570	0	1565	5	0.9157	0.0003	8.851	0.160	8.897	0.017
CCC03	A	H1	12.8	0.3			1565	25	1570	30	0.9315	0.0002	8.917	0.108	8.959	0.002
CCC03	A	H1	12.8	0.2			1590	30	1600	20	0.9298	0.0002	9.009	0.118	8.944	0.004
CCC03	A	H2	13.3	0.3			1805	5	1795	15	0.9339	0.0002	8.778	0.140	8.876	0.014
CCC03	A	H2	14.1	0.5			1785	5	1785	15	0.9333	0.0002	8.809	0.099	8.918	0.033
CCH05	A	H1	13.3	0.3			1550	0	1550	10	0.9262	0.0002	9.127	0.122	8.989	0.019
CCH05	A	H1	13.5	0.5			1610	40	1600	30	0.9280	0.0002	9.027	0.118	8.979	0.017
CCH05	A	H2	14.6	1.2			1655	125	1655	125	0.9242	0.0001	9.109	0.081	9.005	0.004
CCH05	A	H2	15.0	1.0			1735	85	1780	100	0.9255	0.0001	9.037	0.077	8.966	0.007
CCH06	A	H1	14.4	0.1			1655	5	1620	0	0.9298	0.0002	9.068	0.127	9.013	0.010
CCH06	A	H1	15.4	0.1			1715	5	1690	0	0.9302	0.0002	9.048	0.117	9.030	0.011
CCH06	A	H2	13.5	0.7			1695	75	1685	55	0.9287	0.0002	8.924	0.099	8.938	0.011
CCH06	A	H2	13.5	0.7			1740	40	1735	55	0.9326	0.0002	8.718	0.106	8.914	0.015
CCC05	A	H1	16.6	0.4			1535	25	1530	30	0.9337	0.0001	9.221	0.077	9.149	0.008
CCC05	A	H1	16.3	0.2			1585	5	1590	10	0.9368	0.0001	9.043	0.081	9.111	0.011
CCC05	A	H2	17.0	0.3			1685	15	1670	10	0.9301	0.0002	9.199	0.104	9.108	0.021
CCC05	A	H2	17.6	0.4			1800	20	1790	20	0.9357	0.0002	8.896	0.125	9.082	0.012
CCH07	A	H1	19.3	0.3			1545	5	1520	10	0.9369	0.0001	9.332	0.097	9.269	0.016
CCH07	A	H2	19.3	0.4			1750	40	1785	15	0.9440	0.0002	8.966	0.101	9.159	0.016
SDK05-1	B	H1	19.6	0.7	19.7	0.2	1745	65	1765	65	0.9886	0.0003	9.231	0.509	9.192	0.010
SDK05-2	B	H1	23.6	1.7	23.9	0.4	1390	[f]	1505	145	0.9778	0.0006	9.372	0.508	9.469	0.022
CCH01	B	H1	25.4	1.6	22.4	0.3	1800	100	1813	125	0.9799	0.0002	9.298	0.343	9.422	0.032
CCH01	B	H1	25.0	1.4	22.5	0.3	1790	130	1785	125	0.9802	0.0002	9.238	0.320	9.416	0.013
CCH	B	H1	26.3	0.2	20.6	0.0	1745	15	1710	10	0.9716	0.0004	9.526	0.515	9.501	0.006
CCH	B	H1	25.8	0.3	20.4	0.0	1665	15	1665	15	0.9722	0.0003	9.445	0.472	9.497	0.008
Liquid Ni																
CCH04	A	H3	15.5[g]	0.2			2230	30	2230	30	0.8963	0.0004	8.703	0.148		
CCC05	A	H3	22.5[g]	0.1			2480	20	2580	120	0.9342	0.0007	8.979	0.379		

[a]A: Al_2O_3 pressure medium, B: KBr pressure medium.
[b]H1: first heating cycle, H2: second heating cycle, H3: third heating cycle.
[c]Pressure estimated from Ni EOS (Campbell *et al.* 2009).
[d]$\sigma(A)$ represents the error of "*A*."
[e]Pressure estimated from KBr EOS (Dewaele *et al.* 2012).
[f]Temperature measured from one side.
[g]Pressure of liquid Ni was estimated by extrapolating the P–*T* relation obtained from solid Ni data to higher *T*.

High temperature was generated using a double-sided fiber laser heating (wavelength of 1070 nm, SPI Lasers, Ltd). The lasers were converted to flat-top profiles using beam-shaping optics.[18] The size of the laser heating spot was ~22.5–27.5 μm in diameter, which was sufficiently larger than the x-ray beam size as shown in Figs. 1(c) and 1(d). To avoid the interference of glassy carbon (GC) mirror for laser heating with an x-ray beam, the lasers were introduced to the sample from an oblique angle of 20° on both sides (upstream and downstream of the x-ray direction) as shown in the inset of Fig. 2. In all the runs, we confirmed that there was no influence of the GC mirror on the x-ray intensity. The temperature was measured using a spectroradiometric method. The collected thermal radiation spectrum was fitted to the Planck radiation function, and the temperatures on both sides were obtained. The experimental temperatures listed in Table I were taken as the average of the temperatures at the upstream and downstream sides. The temperature errors were derived from the difference in temperature between the front and rear sides and temperature variation during measurements.

The sample was first compressed to the target pressure and heated to approximately 1500–1700 K (first heating). Then, it was quenched to 300 K. In most of the runs, the sample was reheated at the same position to around 1800 K (second heating) and quenched. In the run for liquid measurement, the sample was reheated again at the same position to above 2000 K (third heating) and quenched. At high temperatures, x-ray transmittance and XRD of the Ni sample were measured at several different temperature conditions. The experimental P–T conditions of the density measurements at high temperatures are listed in Table I. Pressures from Ni and KBr references at room temperature are given in supplementary material Table S1 for comparison.

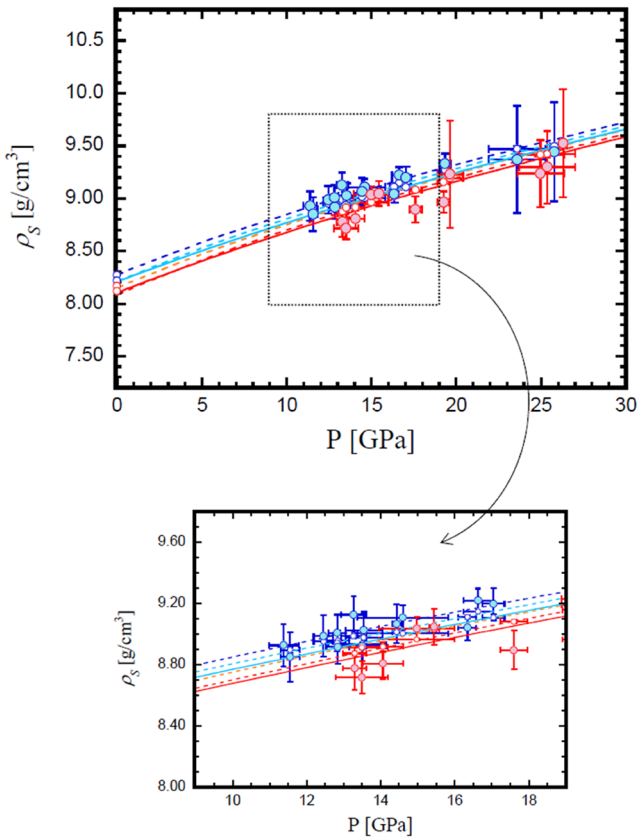

FIG. 3. Density of solid Ni (ρ_S) plotted as a function of pressure. Filled and open circles denote the ρ_s^{Abs} and ρ_s^{XRD}, respectively. Blue and red symbols denote the ρ_S at $T < 1700$ K and that at $T > 1700$ K, respectively. The ρ_S at ambient pressure and high temperatures (1500, 1600, 1700, and 1800 K) calculated from the density at 300 K[20] and thermal expansivity[23] are also plotted. Dashed curves represent the compression curves at high temperatures (blue: 1500 K, light blue: 1600 K, orange: 1700 K, and red: 1800 K) obtained from the elastic properties reported by Ref. 22 with the ρ_S at ambient pressure. Solid curves of light blue and red indicate fitting curves to the ρ_s^{Abs} data of this study with $K' = 4.3$ at 1600 and 1800 K, respectively. The lower panel represents an enlarged image of the dotted square part in the upper panel.

III. RESULTS AND DISCUSSION

A. Density

The experimental conditions of this study and measured densities of solid Ni at high temperatures are summarized in Table I. In this study, we measured the density of solid Ni up to 26.3 GPa and 1805 K. Solid Ni has a face-centered cubic (fcc) structure in all the P–T conditions of this study. The density of solid Ni obtained from the x-ray absorption method was plotted in Fig. 3. The data measured at one or two highest temperature condition(s) just before quenching were used to obtain the densities at high temperatures. In the x-ray absorption method, we obtained the t after quenching in each heating cycle from the measured (I_s/I_0) and (I_{ref}/I_0) with the ρ_s^{XRD} after quenching using Eq. (5). The ρ_s^{Abs} at high T was obtained from measured (I_s/I_0) at high T with t using Eq. (6). We will discuss the validity of the t at high temperature in Sec. III C.

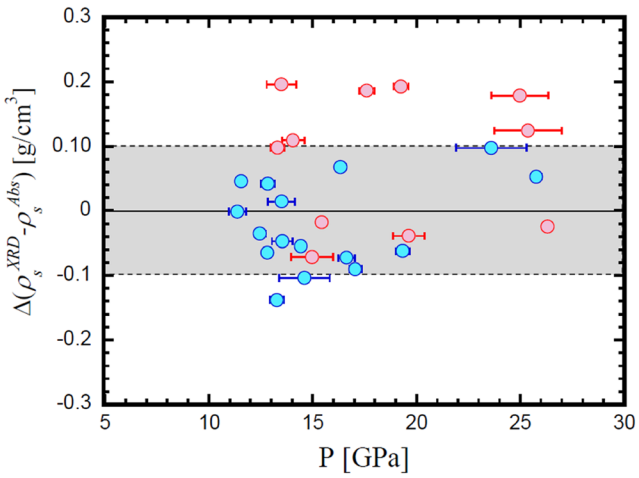

FIG. 4. Difference between ρ_s^{XRD} and ρ_s^{Abs} [$\Delta(\rho_s^{XRD} - \rho_s^{Abs})$] plotted as a function of pressure. Blue and red circles denote the $\Delta(\rho_s^{XRD} - \rho_s^{Abs})$ at $T < 1700$ K and that at $T > 1700$ K, respectively. The gray hutch represents $\Delta(\rho_s^{XRD} - \rho_s^{Abs})$ = ±0.1 g/cm^3, for reference.

TABLE II. Errors of measured quantities.

Run No.	P(Ni) (GPa)	T_{Abs} (K)	$\frac{\partial \rho_s^{Abs}}{\partial \rho_{ref}^{XRD}}\sigma(\rho_{ref}^{XRD})$	$\frac{\partial \rho_s^{Abs}}{\partial (I_s/I_0)}\sigma(I_s/I_0)$	$\frac{\partial \rho_s^{Abs}}{\partial (I_{ref}/I_0)}\sigma(I_{ref}/I_0)$	$\frac{\partial \rho_s^{Abs}}{\partial t}\sigma(t)$	t (μm)	$\sigma(t)$[a] (μm)	ρ_s^{Abs} (g/cm^3)	$\sigma(\rho_s^{Abs})$ (g/cm^3)	ρ_s^{XRD} (g/cm^3)	$\sigma(\rho_s^{XRD})$ (g/cm^3)	$\Delta(\rho_s^{XRD}-\rho_s^{Abs})$[b] (g/cm^3)
CCH04	12.5	1525	0.005	−0.089	0.098	−0.013	22.8	0.08	8.989	0.133	8.954	0.006	−0.036
CCH04	11.4	1490	0.005	−0.096	0.098	−0.013	22.8	0.08	8.930	0.138	8.928	0.010	−0.001
CCH04	11.6	1570	0.009	−0.122	0.102	−0.017	22.2	0.10	8.851	0.160	8.897	0.017	0.046
CCC03	12.8	1565	0.024	−0.066	0.078	−0.026	19.2	0.14	8.917	0.108	8.959	0.002	0.042
CCC03	12.8	1590	0.024	−0.081	0.078	−0.026	19.2	0.14	9.009	0.118	8.944	0.004	−0.065
CCC03	13.3	1805	0.019	−0.125	0.054	−0.028	18.9	0.15	8.778	0.140	8.876	0.014	0.098
CCC03	14.1	1785	0.019	−0.075	0.054	−0.029	18.9	0.15	8.809	0.099	8.918	0.033	0.109
CCH05	13.3	1550	0.014	−0.067	0.099	−0.020	19.1	0.10	9.127	0.122	8.989	0.019	−0.138
CCH05	13.5	1610	0.014	−0.058	0.099	−0.020	19.1	0.10	9.027	0.118	8.979	0.017	−0.047
CCH05	14.6	1655	0.015	−0.066	0.040	−0.018	18.9	0.09	9.109	0.081	9.005	0.004	−0.103
CCH05	15.0	1735	0.015	−0.062	0.040	−0.018	18.9	0.09	9.037	0.077	8.966	0.007	−0.071
CCH06	14.4	1655	0.011	−0.076	0.100	−0.017	18.9	0.09	9.068	0.127	9.013	0.010	−0.055
CCH06	15.4	1715	0.011	−0.058	0.100	−0.017	18.9	0.09	9.048	0.117	9.030	0.011	−0.018
CCH06	13.5	1695	0.010	−0.085	0.047	−0.017	19.9	0.09	8.924	0.099	8.938	0.011	0.014
CCH06	13.5	1740	0.010	−0.093	0.047	−0.016	19.9	0.09	8.718	0.106	8.914	0.015	0.196
CCC05	16.6	1535	0.013	−0.049	0.056	−0.016	18.0	0.08	9.221	0.077	9.149	0.008	−0.069
CCC05	16.3	1585	0.013	−0.054	0.056	−0.015	18.0	0.08	9.043	0.081	9.111	0.011	0.071
CCC05	17.0	1685	0.011	−0.062	0.081	−0.017	19.0	0.09	9.199	0.104	9.108	0.021	−0.090
CCC05	17.6	1800	0.011	−0.094	0.081	−0.015	19.0	0.09	8.896	0.125	9.082	0.012	0.186
CCH07	19.3	1545	0.024	−0.045	0.079	−0.026	17.3	0.12	9.332	0.097	9.269	0.016	−0.082
CCH07	19.3	1750	0.023	−0.058	0.076	−0.024	16.9	0.12	8.966	0.101	9.159	0.016	0.193
SDK05-1	19.6	1745	0.008	−0.775	0.655	−0.087	3.1	0.08	9.231	0.509	9.192	0.010	−0.039
SDK05-2	23.6	1390	0.010	−0.795	0.625	−0.098	6.3	0.18	9.372	0.508	9.469	0.022	0.097
CCH01	25.4	1800	0.017	−0.203	0.274	−0.034	5.8	0.06	9.298	0.343	9.422	0.032	0.124
CCH01	25.0	1790	0.017	−0.162	0.274	−0.033	5.8	0.06	9.238	0.320	9.416	0.013	0.179
CCH	26.3	1745	0.016	−0.313	0.405	−0.058	7.4	0.11	9.526	0.515	9.501	0.006	−0.025
CCH	25.8	1665	0.016	−0.236	0.405	−0.057	7.4	0.11	9.445	0.472	9.497	0.008	0.053

[a] $\sigma(A)$ represents the error of "A."
[b] $\Delta(A-B)$ represents the difference between A and B.

The accuracy of the density of solid Ni from the x-ray absorption method (ρ_s^{Abs}) was evaluated by comparing it with the density of solid Ni obtained from the XRD (ρ_s^{XRD}), which was also plotted in Fig. 3. The difference between ρ_s^{Abs} and ρ_s^{XRD} [$\Delta(\rho_s^{XRD}-\rho_s^{Abs})$] was shown as a function of pressure in Fig. 4. The absolute difference ranges from 0.01%–2.25% (0.001–0.196 g/cm^3), and it is mostly less than 1%. Therefore, in most cases, the ρ_s^{Abs} was consistent with the ρ_s^{XRD} in the present P–T conditions. Although there is no clear variation of the difference between ρ_s^{Abs} and ρ_s^{XRD} with pressure, the difference may tend to be larger at high temperatures.

B. Uncertainty of measured density

The error of the density from the x-ray absorption method [$\sigma(\rho_s^{Abs})$] was estimated from the error propagation of the errors of measured quantities in Eq. (6) as follows:

$$\sigma\left(\rho_s^{Abs}\right)=\sqrt{\left(\frac{\partial \rho_s^{Abs}}{\partial \rho_{ref}^{XRD}}\sigma(\rho_{ref}^{XRD})\right)^2+\left(\frac{\partial \rho_s^{Abs}}{\partial (I_s/I_0)}\sigma(I_s/I_0)\right)^2+\left(\frac{\partial \rho_s^{Abs}}{\partial (I_{ref}/I_0)}\sigma(I_{ref}/I_0)\right)^2+\left(\frac{\partial \rho_s^{Abs}}{\partial t}\sigma(t)\right)^2}. \quad (7)$$

The error of each measured quantity is described below. The $\sigma(\rho_{ref}^{XRD})$ is derived from the error in the lattice volume of the reference material (KBr) obtained by fitting its XRD pattern. The $\sigma(I_s/I_0)$ and $\sigma(I_{ref}/I_0)$ are standard errors of ten measurements of the x-ray intensities (I_s, I_{ref}, and I_0). The $\sigma(t)$ is estimated from the error propagation of the measured quantity errors in Eq. (5) as follows:

$$\sigma(t)=\sqrt{\left(\frac{\partial t}{\partial \rho_s^{XRD}}\sigma(\rho_s^{XRD})\right)^2+\left(\frac{\partial t}{\partial \rho_{ref}^{XRD}}\sigma(\rho_{ref}^{XRD})\right)^2+\left(\frac{\partial t}{\partial (I_s/I_0)}\sigma(I_s/I_0)\right)^2+\left(\frac{\partial t}{\partial (I_{ref}/I_0)}\sigma(I_{ref}/I_0)\right)^2}. \quad (8)$$

The $\sigma(\rho_s^{XRD})$ is derived from the error in the lattice volume of the sample (Ni) at 300 K obtained by fitting the XRD pattern. Each error of measured quantities in Eqs. (7) and (8), $\sigma(t)$ and $\sigma(\rho_s^{Abs})$, is summarized in Table II.

In the condition of P < 20 GPa, the ρ_s^{Abs} from the x-ray absorption method can be determined in the precision of $\sigma(\rho_s^{Abs})$ = 0.07–0.16 g/cm^3 (0.8%–1.8%) and in the accuracy of $|\Delta(\rho_s^{XRD} - \rho_s^{Abs})|$ = 0.001–0.20 g/cm^3 (0.01%–2.2%). On the contrary, at P > 20 GPa, the ρ_s^{Abs} has clearly large errors, as shown in Fig. 3. Although the accuracy is $|\Delta(\rho_s^{XRD} - \rho_s^{Abs})|$ = 0.02–0.18 g/cm^3 (0.26%–1.9%), which is in the similar range of the value at lower pressures, the precision is $\sigma(\rho_s^{Abs})$ = 0.32–0.52 g/cm^3 (3.47%–5.52%), which is much lower than the value at lower pressures. At P < 20 GPa, the sample thickness t ranges from 16.9 ± 0.1–22.8 ± 0.1 μm, while t decreases to 3.1 ± 0.1–7.4 ± 0.1 μm at P > 20 GPa. This suggests that a decrease in t at higher pressures causes a relative increase in $\sigma(t)$ and also in errors of x-ray transmittance [$\sigma(I_s/I_0)$, $\sigma(I_{ref}/I_0)$], thus leading to a lower precision of density [$\sigma(\rho_s^{Abs})$] at higher pressures. To determine the density with high precision [$\sigma(\rho_s^{Abs})$ < 0.1 g/cm^3], the sample thickness t is required to be more than ~15 μm. In addition, increasing the measurement number of I_s, I_{ref}, and I_0 will also improve to reduce the $\sigma(I_s/I_0)$ and $\sigma(I_{ref}/I_0)$.

C. Sample thickness

To evaluate the validity of the sample thickness estimated from the x-ray absorption method as expressed in Eq. (5), we measured

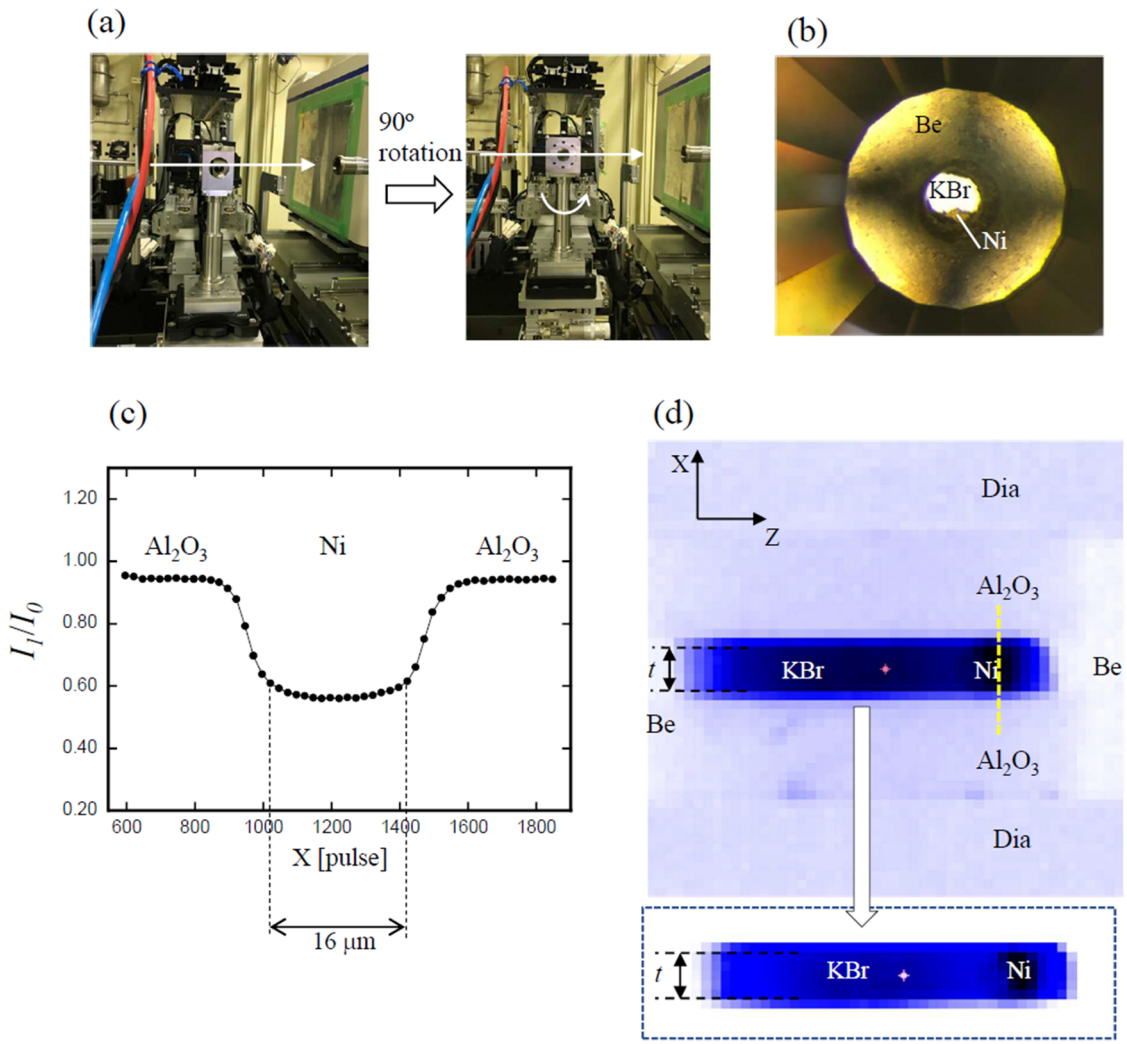

FIG. 5. (a) Setup for the I_1/I_0 measurement through the Be gasket. Left: X-ray is introduced along the compression axis, normal measurement. Right: X-ray is introduced through the gasket in the radial direction. The white arrow shows the x ray. (b) Optical microscope image of the sample chamber at 1.5 GPa. (c) 1D profile of I_1/I_0. Data were collected with a 1 μm step. (d) 2D map of I_1/I_0. The vertical yellow dashed line shows the 1D profile range shown in (c). The bottom area in the dashed rectangle represents the sample chamber with enhanced image contrast.

TABLE III. Lattice volume, thickness, and density of Ni at 300 K and high temperatures.

Run No.	P(Ni) (GPa)	T_{XRD} (K)	V_Q (A^3)	$\sigma(V_Q)$[a] (A^3)	V_T (A^3)	$\sigma(V_T)$ (A^3)	t_Q (μm)	$\sigma(t_Q)$ (μm)	t_T (μm)	$\sigma(t_T)$ (μm)	$\Delta(t_T - t_Q)$[b] (μm)	ρ_Q (g/cm^3)	ρ_T (g/cm^3)	$\Delta(\rho_Q - \rho_T)$ (g/cm^3)
CCH04	12.5	1540	42.74	0.02	43.54	0.03	22.8	0.1	23.0	0.1	0.14	8.989	8.964	0.025
CCH04	11.4	1480	42.74	0.02	43.66	0.05	22.8	0.1	23.0	0.1	0.16	8.930	8.902	0.028
CCH04	11.6	1565	42.66	0.03	43.82	0.08	22.2	0.1	22.4	0.1	0.20	8.851	8.817	0.034
CCC03	12.8	1570	42.34	0.04	43.52	0.01	19.2	0.1	19.3	0.1	0.18	8.917	8.884	0.033
CCC03	12.8	1600	42.34	0.04	43.59	0.02	19.2	0.1	19.3	0.1	0.19	9.009	8.974	0.035
CCC03	13.3	1795	42.47	0.11	43.92	0.07	18.9	0.2	19.2	0.2	0.21	8.778	8.739	0.039
CCC03	14.1	1785	42.47	0.11	43.71	0.16	18.9	0.2	19.1	0.2	0.18	8.809	8.776	0.034
CCH05	13.3	1550	42.11	0.05	43.37	0.09	19.1	0.1	19.3	0.1	0.19	9.127	9.089	0.038
CCH05	13.5	1600	42.11	0.05	43.42	0.08	19.1	0.1	19.3	0.1	0.20	9.027	8.988	0.038
CCH05	14.6	1655	42.08	0.03	43.29	0.02	18.9	0.1	19.1	0.1	0.18	9.286	9.248	0.038
CCH05	15.0	1780	42.08	0.03	43.48	0.03	18.9	0.1	19.1	0.1	0.21	9.215	9.172	0.043
CCH06	14.4	1620	42.35	0.05	43.25	0.05	18.9	0.1	19.0	0.1	0.13	9.068	9.041	0.026
CCH06	15.4	1690	42.35	0.05	43.17	0.05	18.9	0.1	19.0	0.1	0.12	9.048	9.024	0.024
CCH06	13.5	1685	42.35	0.05	43.62	0.05	19.9	0.1	20.1	0.1	0.20	8.924	8.888	0.035
CCH06	13.5	1735	42.35	0.05	43.73	0.08	19.9	0.1	20.1	0.1	0.21	8.718	8.682	0.036
CCC05	16.6	1530	41.59	0.01	42.61	0.04	18.0	0.1	18.1	0.1	0.15	9.218	9.191	0.026
CCC05	16.3	1590	41.59	0.01	42.79	0.05	18.0	0.1	18.2	0.1	0.17	9.040	9.010	0.030
CCC05	17.0	1670	41.62	0.03	42.80	0.10	19.0	0.1	19.2	0.1	0.18	9.199	9.164	0.034
CCC05	17.6	1790	41.62	0.03	42.92	0.06	19.0	0.1	19.2	0.1	0.20	8.896	8.862	0.034
CCH07	19.3	1520	41.19	0.04	42.06	0.07	17.3	0.1	17.4	0.1	0.12	9.332	9.307	0.025
CCH07	19.3	1785	41.21	0.05	42.57	0.08	16.9	0.1	17.1	0.1	0.18	8.966	8.931	0.035
SDK05-1	19.6	1765	40.78	0.05	42.41	0.05	3.1	0.1	3.2	0.1	0.04	9.231	9.185	0.046
SDK05-2	23.6	1505	40.80	0.09	41.17	0.10	6.3	0.2	6.4	0.2	0.02	9.372	9.362	0.010
CCH01	25.4	1813	40.29	0.03	41.38	0.14	5.8	0.1	5.8	0.1	0.05	9.298	9.268	0.030
CCH01	25.0	1785	40.29	0.03	41.40	0.06	5.8	0.1	5.8	0.1	0.05	9.238	9.208	0.030
CCH	26.3	1710	40.86	0.07	41.03	0.03	7.4	0.1	7.4	0.1	0.01	9.526	9.521	0.005
CCH	25.8	1665	40.86	0.07	41.05	0.03	7.4	0.1	7.4	0.1	0.01	9.445	9.439	0.006

[a] $\sigma(A)$ represents the error of "A."
[b] $\Delta(A–B)$ represents the difference between A and B.

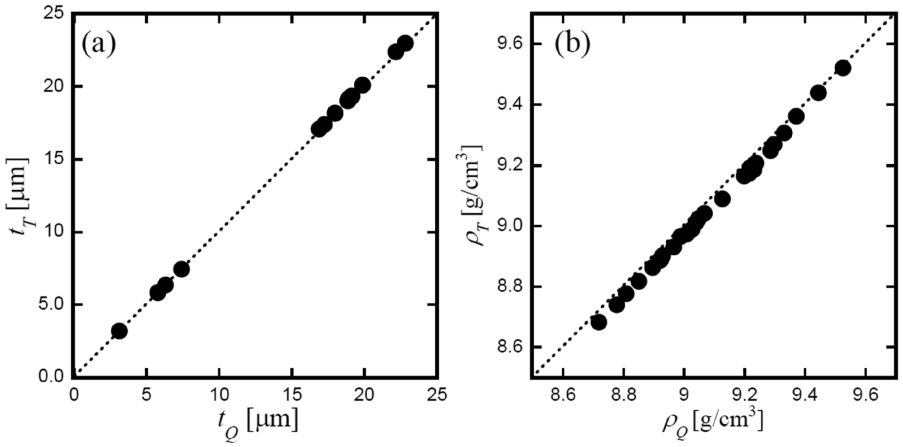

FIG. 6. (a) A comparison between t_T and t_Q. (b) A comparison between ρ_T and ρ_Q. Dotted lines are 1:1 lines. All the values are given in Table III.

the sample thickness directly by using a Be gasket, which has a high x-ray transparency, with the same sample configuration shown in Fig. 1(a) and compared it with the thickness determined from Eq. (5). The measurement setup and cell assembly using a Be gasket are shown in Figs. 5(a) and 5(b). First, x-ray was introduced along the compression axis as normal measurements, and x-ray transmittance (I_1/I_0) and XRD density (ρ^{XRD}) of Ni and KBr were measured at 1.5 GPa. The thickness of the Ni sample was determined to be 15.5–15.8 μm using Eq. (5). Then, the DAC was rotated 90°, and the I_1/I_0 was monitored through the Be gasket in a radial direction. A one-dimensional (1D) profile and 2D map of the I_1/I_0 were measured by moving the DAC stage and shown in Figs. 5(c) and 5(d), respectively. In the 2D map image, the top and bottom of Ni and KBr sandwiched by the Al_2O_3 disk show a parallel interface and the same thickness as shown in Fig. 5(d). This suggests that the thickness of the sample (t_s) is identical to that of the reference (t_{ref}). From the 1D profile of Fig. 5(c), the thickness of the Ni was estimated to ~16 μm. Therefore, the sample thickness determined from Eq. (5) (15.5–15.8 μm) is consistent with the directly measured thickness (~16 μm), indicating that the sample thickness from Eq. (5) used in this study is valid.

The effect of temperature on the sample thickness is also evaluated in this section. The sample thickness at high temperature (t_T) can be estimated as follows, assuming

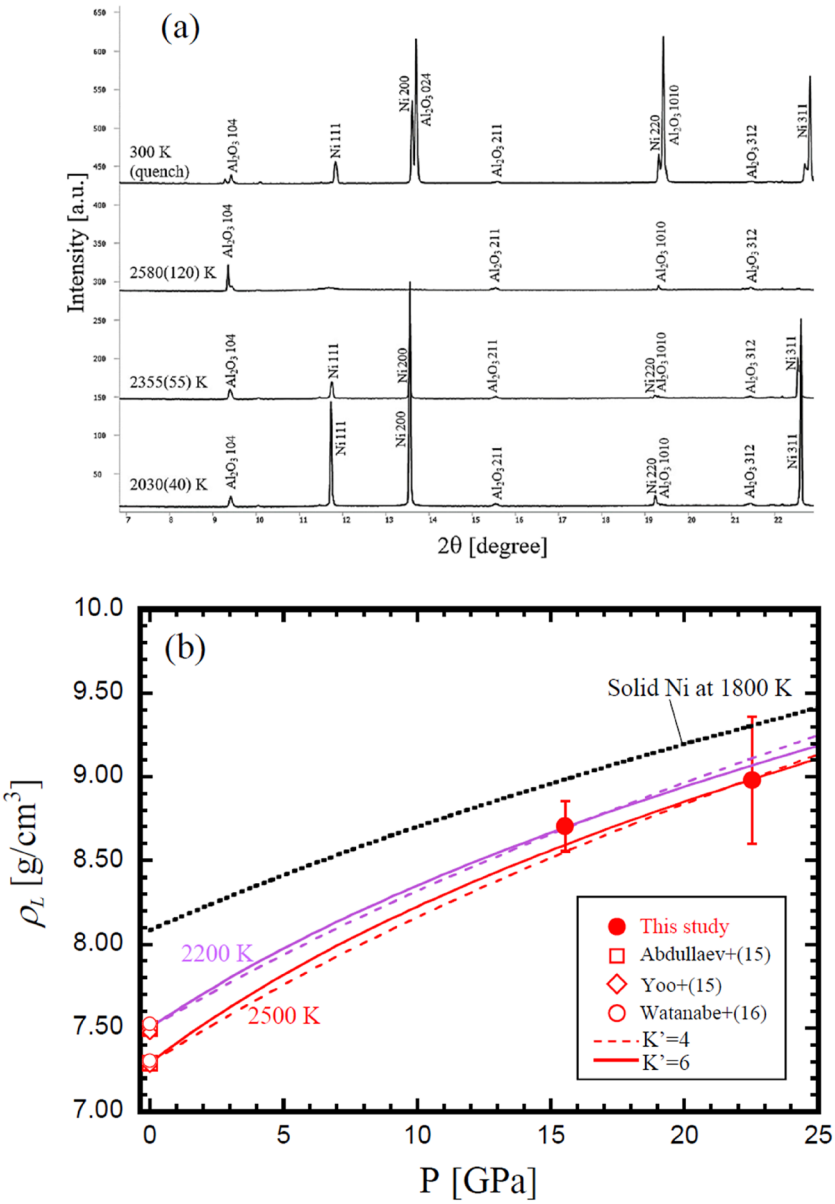

FIG. 7. (a) XRD patterns in the 3rd heating cycle of run CCC05. Al_2O_3 peaks correspond to the peaks from the pressure medium. The diffraction peaks of the Ni sample disappeared at 2580 ± 120 K (in addition, the background level increased at around 2θ = 11.7°) and reappeared after quenching, suggesting that the sample was molten at 2580 ± 120 K. The XRD pattern of liquid Ni at 2580 ± 120 K with an enlarged vertical scale is shown in supplementary material, Fig. S1. (b) Density of liquid Ni (ρ_L) as a function of pressure. The filled symbol indicates the ρ_L at 15.4 GPa, 2230 K, and 22.5 GPa, 2480 K of this study. Open symbols represent the ρ_L at ambient pressure and 2200, 2500 K calculated from their density data at lower temperatures and their temperature dependence.[24–26] The black dotted curve represents the compression curve of solid Ni at 1800 K.[22] Dashed and solid curves represent the fitted compression curves of liquid Ni, assuming K' = 4 and 6, respectively (purple: 2200 K and red: 2500 K).

that the sample volume expands isotropically at high temperatures,

$$t_T = \left(\frac{V_T}{V_Q}\right)^{\frac{1}{3}} t_Q, \quad (9)$$

where V_T, V_Q, and t_Q denote the lattice volume of the sample at high temperature, that at 300 K after quench, and the sample thickness at 300 K after quench, respectively. All the parameters on the right hand side of Eq. (9) were measured in this study. These values and t_T are listed in Table III. The error of t_T [$\sigma(t_T)$] was obtained from an error propagation of $\sigma(V_T)$, $\sigma(V_Q)$, and $\sigma(t_Q)$ shown in Table III. A comparison between t_T and t_Q is shown in Fig. 6(a). In Fig. 6(a), the estimated t_T and t_Q were almost on the 1:1 line (equality line), and the difference between t_T and t_Q is 0.01–0.21 μm. Therefore, the sample thickness at high temperature and that after quenching were found to be only 0.1%–1.3% different in the present experimental conditions.

The densities ρ_T and ρ_Q were estimated from Eq. (6) using the same transmittance data (I_s/I_0) at high temperature with t_T and t_Q, respectively. The density ρ_s^{Abs} estimated in Sec. III A and plotted in Fig. 3 corresponds to the ρ_Q. The ρ_T and ρ_Q were compared in Fig. 6(b). The difference between ρ_T and ρ_Q ranges from 0.01–0.05 g/cm^3 (0.05%–0.50%), suggesting that these differences are within the density error. Therefore, the density using t_Q is almost identical to the density using t_T, and the effect of temperature on the sample thickness is quite minor between high temperature and after quenching.

However, the pressure in the sample chamber changes between high temperature and after quenching. This is most likely to be derived from the disappearance of the thermal pressure contribution after the quench. The experimental pressures at high temperatures, P(Ni), were estimated from the measured lattice volume of the Ni sample and its equation of state. In the experiment using the KBr pressure medium (B type cell), the pressure can also be estimated from the measured lattice volume of KBr at high temperatures, which we call P(KBr). P(Ni) and P(KBr) are listed in Table I. Although P(Ni) and P(KBr) show some gap, both P(Ni) and P(KBr) at high temperatures reduced to some extent after quenching. This suggests that temperature contributes to increasing the thermal pressure rather than thermal expansion in the sample configuration of this study.

D. Elastic properties of solid Ni and density of liquid Ni

The density data of solid Ni measured from the x-ray absorption method in this study were fitted using the third-order Birch–Murnaghan equation of state to obtain elastic properties. In the fitting, densities at ambient pressure and high temperatures (1500, 1600, 1700, 1800 K) calculated from the density of 8.9072 g/cm^3 at 300 K[20] and thermal expansivity of $\alpha = 6.18 \times 10^{-5}$ K^{-1}[23] were used. Since the density data are distributed in a limited pressure range, the K' was fixed to 4.0 or 4.3.[22] The fitting curve is shown as solid curves in Fig. 3, and the isothermal bulk modulus at ambient pressure (K_{T0}) was obtained to be 176 ± 23 GPa for $K' = 4.0$ and 177 ± 24 GPa for $K' = 4.3$. The K_{T0} in this study is slightly smaller than the reported value (K_{T0} = 179 GPa).[21] However, the K_{T0} in this study has a large fitting error. To constrain the K_{T0} more accurately, we need to increase the density data in the wide pressure range.

The density of liquid Ni (ρ_L) was measured at 15.5–22.5 GPa and 2230–2480 K and determined to be ρ_L = 8.70 ± 0.15 and 8.98 ± 0.38 g/cm^3. The melting of the Ni sample was confirmed from the disappearance of XRD peaks shown in Fig. 7(a). (XRD pattern of liquid Ni with enlarged vertical scale is shown in supplementary material, Fig. S1.) The experimental pressure of liquid Ni was estimated by extrapolating the P–T relation, obtained from solid Ni in the third heating cycle of the same run, to higher T (2230 and 2480 K). The measured density of liquid Ni at 15.5 and 22.5 GPa was plotted together with that at ambient pressure[24–26] in Fig. 7(b). Based on the ρ_L at ambient pressure and high pressures, the isothermal compression curve of liquid Ni at 2200 K is roughly estimated assuming $K' = 4$ and 6 [Fig. 7(b)]. The obtained $K_{2200K,0}$ = 78.5 ± 1.0 GPa for $K' = 4$ and $K_{2200K,0}$ = 67.5 ± 0.7 GPa for $K' = 6$. The liquid compression curves are likely to have a steeper slope compared to the compression curve of solid Ni [Fig. 7(b)], suggesting that liquid Ni is more compressible. By using the x-ray absorption method with the laser heated DAC developed in this study, we can measure the density of liquid Ni. Therefore, we expect that densities and the equation of state of various liquids can be determined by this method in future studies.

IV. CONCLUSION

In this study, we developed density measurement using the x-ray absorption method combined with laser heated DAC. The density of solid Ni was measured up to the pressure and temperature conditions of 26 GPa and 1800 K. The accuracy and precision of the present method were verified from the measured density of solid Ni by comparison with the density obtained from XRD data and evaluation of the uncertainties, respectively. For samples with a thickness of >17 μm, the density of solid Ni can be determined with an accuracy of 0.001–0.20 g/cm^3 (0.01%–2.2%) and with a precision of 0.07–0.16 g/cm^3 (0.8%–1.8%). Therefore, it is confirmed that the density of solid Ni can be determined with high accuracy and precision by this method. A sample thickness of at least ~15 μm is required.

The sample thickness at high temperature and that after quenching were only 0.1%–1.3% different in the present experimental conditions and sample configuration. This suggests that the effect of temperature on the sample thickness is quite minor between high temperature and after quenching. Instead, the experimental pressure varies between high temperature and after quenching.

The K_{T0} of solid Ni at 1600 K was determined to be 176 ± 23 GPa for $K' = 4.0$ and 177 ± 24 GPa for $K' = 4.3$ from the fitting of measured density. However, we need more density data to reduce the error of the K_{T0}. The density of liquid Ni was also measured at 15.5–22.5 GPa and 2230–2480 K, and it was obtained to be 8.70 ± 0.15–8.98 ± 0.38 g/cm^3.

In conclusion, by using the x-ray absorption method combined with the laser heated DAC developed in this study, the measurable temperature range of the x-ray absorption method expanded significantly from 720 to 2480 K. Since the x-ray absorption method provides the density more simply and directly without any sophisticated analytical requirements, the present method is a useful and powerful tool for obtaining the densities of various liquids at high

pressures. This is important for accurately understanding the density and elastic behavior of liquid materials at extreme conditions, which is closely related to the formation and evolution processes of planetary deep interiors.

SUPPLEMENTARY MATERIAL

The supplementary material to this article can be found online. The supplementary material contains a table of pressures estimated from the Ni sample and KBr reference at room temperature (Table S1) and an XRD pattern of the liquid Ni at 2580 ± 120 K with an enlarged vertical scale from [Figs. 7(a) and (S1)].

ACKNOWLEDGMENTS

The authors acknowledge H. Kadobayashi, K. Kurosaka, and T. Kato for technical assistance. The authors also acknowledge H. Fukui for kindly providing the Be gasket. The authors are grateful to S. Urakawa for his constructive discussions and to the two anonymous reviewers for their constructive comments and useful suggestions. This work was partly supported by Grants-in-Aid for scientific research from the Ministry of Education, Culture, Sport, and Science and Technology (MEXT) of the Japanese Government to H.T. (Grant No. 20H02008). The synchrotron radiation experiments were performed under contract with the SPring-8 facility (Proposal Nos. 2019B1587, 2020A1325, 2020A1340, 2021A1517, 2021B1658, 2022A1450, 2022B1510, 2023A1440, 2023B1495, and 2024A1470).

AUTHOR DECLARATIONS

Conflict of Interest

The authors have no conflicts to disclose.

Author Contributions

Hidenori Terasaki: Conceptualization (lead); Data curation (lead); Formal analysis (lead); Writing – original draft (lead). **Hiroyuki Kamina**: Data curation (supporting); Formal analysis (supporting). **Saori I. Kawaguchi**: Data curation (supporting); Methodology (supporting). **Tadashi Kondo**: Data curation (supporting); Methodology (supporting). **Ko Morioka**: Data curation (supporting); Formal analysis (supporting). **Ryo Tsuruoka**: Data curation (supporting); Formal analysis (supporting). **Moe Sakurai**: Data curation (supporting). **Akira Yoneda**: Data curation (supporting). **Seiji Kamada**: Conceptualization (supporting); Data curation (supporting). **Naohisa Hirao**: Data curation (supporting).

DATA AVAILABILITY

The data that support the findings of this study are available from the corresponding author upon reasonable request.

REFERENCES

[1]T. Sakamaki, A. Suzuki, E. Ohtani, H. Terasaki, S. Urakawa, Y. Katayama, K. Funakoshi, Y. Wang, J. W. Hernlund, and M. Ballmer, "Ponded melt at the boundary between the lithosphere and asthenosphere," Nat. Geosci. **6**, 1041–1044 (2013).

[2]D. Breuer, T. Rueckriemen, and T. Spohn, "Iron snow, crystal floats, and inner-core growth: Modes of core solidification and implications for dynamos in terrestrial planets and moons," Prog. Earth Planet. Sci. **2**, 39 (2015).

[3]H. Terasaki and K. Nishida, "Density and elasticity measurements for liquid materials," in *Magmas under Pressure: Advances in High-Pressure Experiments on Structure and Properties of Melts*, edited by Y. Kono and C. Sanloup (Elsevier, 2018), pp. 237–255.

[4]Y. Katayama, K. Tsuji, J.-Q. Chen, N. Koyama, T. Kikegawa, K. Yaoita, and O. Shimomura, "Density of liquid tellurium under high pressure," J. Non-Cryst. Solids **156–158**, 687–690 (1993).

[5]C. Sanloup, F. Guyot, P. Gillet, G. Fiquet, M. Mezouar, and I. Martinez, "Density measurements of liquid Fe–S alloys at high-pressure," Geophys. Res. Lett. **27**, 811–814, https://doi.org/10.1029/1999gl008431 (2000).

[6]H. Terasaki, K. Nishida, Y. Shibazaki, T. Sakamaki, A. Suzuki, E. Ohtani, and T. Kikegawa, "Density measurement of Fe_3C liquid using X-ray absorption image up to 10 GPa and effect of light elements on compressibility of liquid iron," J. Geophys. Res. **115**, B06207, https://doi.org/10.1029/2009JB006905 (2010).

[7]T. Sato and N. Funamori, "Sixfold-coordinated amorphous polymorph of SiO_2 under high pressure," Phys. Rev. Lett. **101**, 255502 (2008).

[8]S. Petitgirard, W. J. Malfait, R. Sinmyo, I. Kupenko, L. Hennet, D. Harries, T. Dane, M. Burghammer, and D. C. Rubie, "Fate of $MgSiO_3$ melts at core-mantle boundary conditions," Proc. Natl. Acad. Sci. U. S. A. **112**, 14186–14190 (2015).

[9]G. Shen, N. Sata, N. Taberlet, M. Newville, M. L. Rivers, and S. R. Sutton, "Melting studies of indium: Determination of the structure and density of melts at high pressures and high temperatures," J. Phys.: Condens. Matter **14**, 10533–10540 (2002).

[10]Y. Takubo, H. Terasaki, T. Kondo, S. Mitai, S. Kamada, T. Kikegawa, and A. Machida, "Development of density measurement for metals at high pressures and high temperatures using X-ray absorption imaging combined with externally heated diamond anvil cell," C. R. Geosci. **351**, 182–189 (2019).

[11]R. Tsuruoka, H. Terasaki, S. Kamada, F. Maeda, T. Kondo, N. Hirao, S. I. Kawaguchi, I. Yamada, S. Urakawa, and A. Machida, "Density and elastic properties of liquid gallium up to 10 GPa using X-ray absorption method combined with externally heated diamond anvil cell," High Pressure Res. **41**, 379–391 (2021).

[12]H. Samuel, M. Drilleau, A. Rivoldini, Z. Xu, Q. Huang, R. F. Garcia, V. Lekić, J. C. E. Irving, J. Badro, P. H. Lognonné, J. A. D. Connolly, T. Kawamura, T. Gudkova, and W. B. Banerdt, "Geophysical evidence for an enriched molten silicate layer above Mars's core," Nature **622**, 712–717 (2023).

[13]J. H. Eggert, G. Weck, P. Loubeyre, and M. Mezouar, "Quantitative structure factor and density measurements of high-pressure fluids in diamond anvil cells by x-ray diffraction: Argon and water," Phys. Rev. B **65**, 174105 (2002).

[14]G. Morard, J. Siebert, D. Andrault, N. Guignot, G. Garbarino, F. Guyot, and D. Antonangeli, "The Earth's core composition from high pressure density measurements of liquid iron alloys," Earth Planet. Sci. Lett. **373**, 169–178 (2013).

[15]Y. Kuwayama, G. Morard, Y. Nakajima, K. Hirose, A. Q. R. Baron, S. I. Kawaguchi, T. Tsuchiya, D. Ishikawa, N. Hirao, and Y. Ohishi, "Equation of state of liquid iron under extreme conditions," Phys. Rev. Lett. **124**, 165701 (2020).

[16]S. I. Kawaguchi, G. Morard, Y. Kuwayama, K. Hirose, N. Hirao, and Y. Ohishi, "Density determination of liquid iron-nickel-sulfur at high pressure," Am. Mineral. **107**, 1254–1261 (2022).

[17]C. Sanloup, J. W. E. Drewitt, Z. Konôpková, P. Dalladay-Simpson, D. M. Morton, N. Rai, W. van Westrenen, and W. Morgenroth, "Structural change in molten basalt at deep mantle conditions," Nature **503**, 104–107 (2013).

[18]N. Hirao, S. I. Kawaguchi, K. Hirose, K. Shimizu, E. Ohtani, and Y. Ohishi, "New developments in high-pressure X-ray diffraction beamline for diamond anvil cell at SPring-8," Matter Radiat. Extremes **5**, 018403 (2020).

[19]Y. Seto, D. Nishio-Hamane, T. Nagai, and N. Sata, "Development of a software suite on X-ray diffraction experiments," Rev. High Pressure Sci. Technol. **20**, 269–276 (2010).

[20]A. Dewaele, M. Torrent, P. Loubeyre, and M. Mezouar, "Compression curves of transition metals in the Mbar range: Experiments and projector augmented-wave calculations," Phys. Rev. B **78**, 104102 (2008).

[21] A. Dewaele, A. B. Belonoshko, G. Garbarino, F. Occelli, P. Bouvier, M. Hanfland, and M. Mezouar, "High-pressure-high-temperature equation of state of KCl and KBr," Phys. Rev. B **85**, 21405 (2012).
[22] A. J. Campbell, L. Danielson, K. Righter, C. T. Seagle, Y. Wang, and V. B. Prakapenka, "High pressure effects on the iron–iron oxide and nickel–nickel oxide oxygen fugacity buffers," Earth Planet. Sci. Lett. **286**, 556–564 (2009).
[23] A. Kamiya, H. Terasaki, and T. Kondo, "Precise determination of the effect of temperature on the density of solid and liquid iron, nickel, and tin," Am. Mineral. **106**, 1077–1082 (2021).
[24] R. N. Abdullaev, Yu. M. Kozlovskii, R. A. Khairulin, and S. V. Stankus, "Density and thermal expansion of high purity nickel over the temperature range from 150 K to 2030 K," Int. J. Thermophys. **36**, 603–619 (2015).
[25] H. Yoo, C. Park, S. Jeon, S. Lee, and G. W. Lee, "Uncertainty evaluation for density measurements of molten Ni, Zr, Nb and Hf by using a containerless method," Metrologia **52**, 677–684 (2015).
[26] M. Watanabe, M. Adachi, and H. Fukuyama, "Densities of Fe–Ni melts and thermodynamic correlations," J. Mater. Sci. **51**, 3303–3310 (2016).